Energy & Environmental Science

Accepted Manuscript

ROYAL SOCIETY OF CHEMISTRY

www.rsc.org/ees

Predicting the Solar Thermochemical Water Splitting Ability and Reaction Mechanism of Metal Oxides: a Case Study of the Hercynite Family of Water Splitting Cycles

Christopher L. Muhich[a†], Brian D. Ehrhart[a], Vanessa A. Witte[a], Samantha L. Miller[a], Eric N. Coker[c], Charles B. Musgrave[a,b*], and Alan W. Weimer[a*]

[a]Department of Chemical and Biological Engineering, University of Colorado, Boulder, Colorado 80309, USA

[b]Department of Chemistry and Biochemistry, University of Colorado, Boulder, Colorado 80309, USA

[c]Sandia National Laboratories, Albuquerque, New Mexico 87123, USA

[*]Corresponding Author: Email addresses: Charles.Musgrave@colorado.edu and Alan.Weimer@colorado.edu

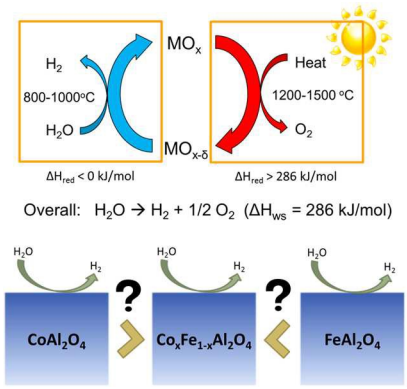

Summary Sentence:

We report and validate a method for predicting the solar thermal water splitting abilities of novel materials using easily calculated quantities.

Summary Paragraph:

We develop and validate a method for predicting the solar thermal water splitting ability of new materials and their reaction mechanism using only the reduction energies of the novel material and a benchmark material. This method relies only upon the material's reduction energy, which is easily obtainable from DFT calculations and does not require the calculation of reduction entropies, which are very challenging to determine with sufficient accuracy. We then demonstrate this method by predicting the STWS abilities of two novel materials, $FeAl_2O_4$ and $CoAl_2O_4$, using the previously demonstrated doped hercynite ($Co_{0.33}Fe_{0.66}Al_2O_4$) material as the benchmark material. We computationally predict that the aluminate cycles operate via an O-vacancy mechanism rather than the previously suggested stoichiometric mechanism and that they produce H_2 in a 1.0 to 0.7 to 2×10^{-4} ratio for $FeAl_2O_4$, $Co_{0.33}Fe_{0.66}Al_2O_4$ and $CoAl_2O_4$, respectively. We validated these predictions experimentally, where XRD analysis confirms that an O-vacancy mechanism is operative and water splitting experiments measure relative H_2 production capacities of 1.0 to 0.6 to 0.0 for $FeAl_2O_4$, $Co_{0.33}Fe_{0.66}Al_2O_4$ and $CoAl_2O_4$, respectively.

Abstract

A screening method is developed to determine the viability of candidate redox materials to drive solar thermal water splitting (STWS) and the mechanism by which they operate using only the reduction enthalpy of the material. This method is applied to the doped-hercynite water splitting cycle, as well as $FeAl_2O_4$ and $CoAl_2O_4$, materials which have not been previously experimentally demonstrated for STWS. Density functional theory (DFT) calculations of reduction energies coupled with our screening method predict H_2 production capacities for iron and cobalt aluminate spinels to be in the order $FeAl_2O_4$ > $Co_{0.5}Fe_{0.5}Al_2O_4$ > $CoAl_2O_4$ with relative H_2 production capacity ratios of approximately 1.0 to 0.7 to 2×10^{-4}, respectively. Experimental measurements for 1500/1350°C redox temperatures validate the H_2 production capacity predicted by the screening method by demonstrating H_2 production ratios of 1.0 to 0.6 to 0. Un-doped hercynite ($FeAl_2O_4$) is shown to be a viable STWS material for the first time with a higher H_2 production capacity than traditional doped-hercynite materials. Theory and experiments show that redox of the aluminate family of spinel materials operates via an O-vacancy mechanism rather than a stoichiometric one, which is more typical for ferrites. The screening approach is generally useful for predicting the ability of new complex materials to drive STWS and the mechanism by which they operate, thus, providing a method to identify promising new candidate STWS materials.

1.0 Introduction

Solar energy has the potential to provide the energy needs of a growing and energy demanding population; however, the capture, storage, and distribution of this dispersed resource remain a challenge. Solar thermochemical water splitting (STWS) is a promising route to efficiently capture and store this resource because it converts radiation from the entire solar spectrum into the chemical energy stored in the bonds of an energy dense fuel, H_2.[1-6] Because the entire solar spectrum is used, STWS has one of the highest theoretical solar to hydrogen efficiencies of processes reported, including solar driven electrolysis and photo-electrochemical water splitting.[2] In two-step metal oxide based STWS, a metal oxide is heated using concentrated solar thermal energy to a temperature at which it reduces, generating O_2. Subsequently, H_2O is introduced to the system to re-oxidize the material and generate H_2.[2, 4, 7, 8] STWS operation can be categorized by the temperature difference between the reduction and oxidation steps. Conventional STWS operates in a temperature swing water splitting (TSWS) mode in which water splitting is driven solely by a temperature difference of at least ~150°C. We recently demonstrated that significant H_2 could be produced by an isothermal water splitting (ITWS) redox cycle in which the reduction and oxidation steps are performed at the same temperature, and an oxygen chemical potential difference drives water splitting.[7] STWS can also be driven by combinations of temperature and chemical potential differences using temperature changes between the reduction and oxidation steps of less than ~150°C, which we consider near-isothermal water splitting (NITWS).[9]

The ideal material for efficiently driving STWS has not yet been identified, even though a large number of materials have been examined. To be a STWS material, a candidate material must undergo both reduction and water oxidation; to be a practical STWS material, it must

reduce at temperatures which are achievable using concentrated sunlight and at which reactor containment materials do not degrade (<~1700°C). The assessment of STWS materials and cycles has generally been undertaken by one of two approaches: 1) evaluating a set of previously proposed water splitting cycles for their practical viability;[8, 10-12] or 2) identifying novel materials from a broad set of candidates by predicting their ability to drive STWS.[13,14] Because an optimal STWS material or cycle has not yet been identified, we focus here on the latter of these two approaches, which we call "STWS materials screening".[13, 14]

Novel materials are traditionally screened by calculating whether a candidate material decomposes at achievable reduction temperatures and whether water re-oxidizes the decomposed material back to the original oxide using standard enthalpies and entropies of formation of the oxidized and reduced compounds.[13,14] The vast majority of simple binary metal oxides (M_xO_y where M is a metal) have been examined for use as STWS materials under the assumption that they operate via volatile or non-volatile stoichiometric mechanisms.[8, 10-14] In the stoichiometric reaction mechanism, the active material decomposes to a reduced phase to produce a stoichiometric quantity of O_2, as exemplified by the mixed metal ferrite cycle[4] shown in Equations 1 and 2.

$$CoFe_2O_4 \rightarrow CoO + 2FeO + \frac{1}{2} O_2 \quad (1)$$

$$CoO + 2FeO + H_2O \rightarrow CoFe_2O_4 + H_2 \quad (2)$$

Every mole of $CoFe_2O_4$ that reacts produces a stoichiometric half mole of O_2. The amount of $CoFe_2O_4$ that undergoes reduction depends on the reaction temperature and oxygen partial pressure.

As the names suggest, the difference between the volatile and non-volatile stoichiometric chemistries is the phase of the reduced product; a gas in the case of the volatile stoichiometric mechanism, or a liquid or solid in the case of the non-volatile stoichiometric mechanism. These reaction mechanisms are convenient for screening candidate STWS materials because decomposition and oxidation reaction enthalpies and entropies of binary oxide materials are easily calculated from the heats of formation of the reduced and oxidized forms, which are commonly tabulated in online databases. However, researchers have only identified a few potential STWS materials using this screening method. Chief among these are ZnO, SnO_2, and Fe_3O_4, but none of these are particularly promising because they generate gaseous and liquid reduction products and require high reduction temperatures.[4, 15-17] This screening approach has over looked new STWS materials because it can be difficult to obtain the decomposition energetics of novel complex metal oxides, and, more importantly, this method assumes that the potential STWS materials operate by a stoichiometric chemistry.

Ceria (CeO_2), perovskite ($Sr_xLa_{1-x}Mn_yAl_{1-y}O_3$), and doped-hercynite ($Co_xFe_{1-x}O_4/Al_2O_3$) cycles have been proposed as candidate commercial STWS materials and show more promise than the ZnO, SnO_2, and Fe_3O_4 cycles due to their lower required reaction temperatures and their solid-state reduction products.[9, 18-22] These cycles have only recently become of interest and were not identified by previous screening methods for a variety of possible reasons, including their non-standard reaction mechanisms, more complex compositions, or because O-vacancy materials were at first suggested to produce too little H_2 per unit mass to be economical.[11] The low temperature (T_{red} ≈1500-1700°C) CeO_2 O-vacancy cycle was not identified by screening methods because CeO_2 was originally only screened as a stoichiometric material; however, it does not decompose to Ce_2O_3 at temperatures below 2000°C,[22] which is too high for practical

STWS. However, while attempting to lower the CeO_2 decomposition temperature through doping with other metal oxides Kaneko *et al.* discovered that CeO_2 splits water after reduction at 1500°C and that at this temperature the CeO_2 cycle operates by an O-vacancy mechanism.[23] As the name suggests, reduction of O-vacancy materials produces oxygen vacancies within the lattice of the host material without it decomposing into a different phase; these vacancies are subsequently filled during oxidation by the O atoms of split H_2O molecules.[23] Equations 3 and 4 show that, for every mole of CeO_2 reduced, δ/2 moles of O_2 and δ moles of oxygen vacancies form, where the extent of non-stoichiometry (δ) depends on the reduction temperature and oxygen partial pressure.

$$CeO_2 \rightarrow CeO_{2-\delta} + \frac{\delta}{2} O_2 \quad (3)$$

$$CeO_{2-\delta} + \delta H_2O \rightarrow CeO_2 + \delta H_2 \quad (4)$$

It is difficult to screen for new O-vacancy STWS materials because the energy used to split water is not stored in a second, reduced phase for which heats and entropies of formation are readily available. Instead the water splitting energy is stored in O-vacancies for which the concentrations, reduction energy, and thermodynamic effects are not generally tabulated in thermodynamic databases.

Perovskite based STWS cycles have also only recently been demonstrated using $Sr_xLa_{1-x}Mn_yAl_{1-y}O_3$.[17] Traditional screening methods based on stoichiometric reaction mechanisms did not consider these materials because their complex compositions make it difficult to determine their reduction products and the associated reaction thermodynamics, which are required for screening. Additionally, these materials have been shown to operate by an O-vacancy mechanism[19, 21] and, thus, they do not decompose at practical STWS temperatures. Therefore,

even if $Sr_xLa_{1-x}Mn_yAl_{1-y}O_3$ had been screened, it would likely have been rejected for requiring impractically high decomposition temperatures. While the $Sr_xLa_{1-x}MnO_3$ based cycles were the first perovskite cycles proposed,[19, 24] other cycles have been suggested such as $CaTi_xFe_{1-x}O_3$, and $Ba_xSr_{1-x}Co_yFe_{1-y}O_3$, which indicates that other perovskites that can drive STWS likely exist.[21, 25] These materials were not identified by a systematic screening method. If perovskites are to be thoroughly examined for their use in STWS, a screening method appropriate for analyzing O-vacancy materials must be developed which can quickly and accurately predict the STWS ability of candidate materials.

Similarly, the doped-hercynite cycle was only identified relatively recently. In 2010, Scheffe *et al.*[20] reported a new STWS cycle based on a mixture of $CoFe_2O_4$ and Al_2O_3 which was named the "doped-hercynite cycle" as it was assumed to operate similarly to cobalt ferrite through the formation and decomposition of cobalt aluminate and hercynite ($FeAl_2O_4$), as shown in Equations 5 and 6.

$$CoFe_2O_4 + 3Al_2O_3 \rightarrow CoAl_2O_4 + 2FeAl_2O_4 + \frac{1}{2}\,O_2 \qquad (5)$$

$$CoAl_2O_4 + 2FeAl_2O_4 + H_2O \rightarrow CoFe_2O_4 + 3Al_2O_3 + H_2 \qquad (6)$$

Scheffe *et al.*[20] demonstrated the doped-hercynite cycle experimentally and used the FACTSage™ Gibbs free energy minimization software package[26] to predict the thermodynamic end states of the material. Additionally, they used FACTSage™ to estimate the O_2 evolution produced from the reduction of a Fe_3O_4 and Al_2O_3, and a $CoFe_2O_4$ and ZrO_2 mixture and found them to evolve less O_2 than the reduction of the $CoFe_2O_4$ and Al_2O_3 mixture for temperatures < 1450°C. However, they did not investigate the water splitting ability of a mixed Fe_3O_4 and Al_2O_3 system experimentally or computationally.

As with the case of the perovskites, the doped-hercynite cycle was not considered by previous screening techniques, possibly because researchers screening STWS materials had previously only considered binary metal oxides while hercynite is a more complex material. Because screening for STWS materials with these complex reaction mechanisms and structures is difficult, no new cycles based on the doped-hercynite cycle have been demonstrated.

The doped-hercynite STWS cycle is particularly promising as it produces significant quantities of H_2 and requires a low reduction temperature (1200°C), which was the lowest reduction temperature of any two-step metal oxide based STWS cycle previously reported. The 1200°C reduction temperature is ~200°C lower than the required reduction temperature of traditional ferrite cycles and ~300°C lower than that required for the ceria and ZnO cycles.[9, 20, 27, 28] Additionally, the aluminate reduction products do not melt at temperatures under 1600°C. Therefore, the doped-hercynite cycle can operate over a wide range of reduction temperatures without melting or sintering which are problems that plague other ferrite-based cycles because of the less than 150°C difference in the reduction and melting temperature of the traditional ferrite cycle.[17] While promising, the reaction mechanism of the doped-hercynite cycle has not been fully investigated.

The majority of the materials potentially involved in the doped-hercynite cycle are spinels, including Fe_3O_4, Co_3O_4, $FeAl_2O_4$, $CoAl_2O_4$, and mixtures thereof. Spinels are a class of materials with a generic composition of AB_2O_4, where A and B possess formal oxidation states of +2 and +3, and take on either a normal or inverse structure. In normal spinels, the A cations occupy tetrahedral sites while the B cations occupy octahedral sites, as shown in Supplemental Information (SI) Figure SI1a. In inverse spinels, half of the B cations occupy the tetrahedral sites while the remaining B cations and all of the A cations occupy octahedral sites, as shown in SI

Figure SI1b. Most spinels are not fully normal or inverse, but rather are a mixture of the two. The degree to which a spinel possesses an inverse or normal structure is quantified by the inversion parameter X, where X=0 indicates a completely normal spinel and X=1 indicates a completely inverse spinel. Of the materials of interest here, $FeAl_2O_4$, and $CoAl_2O_4$ are mostly normal while $CoFe_2O_4$ is a mostly inverse spinel.[29]

In this work, we describe a method to predict the reaction mechanism and the capability of complex materials to split water. We apply this method in conjunction with density functional theory (DFT)[12,13] to determine the reaction mechanism of the doped-hercynite cycle and analyze the previously undemonstrated $FeAl_2O_4$ and $CoAl_2O_4$ oxides for use in STWS. We validate the computational findings using H_2 generation experiments, X-ray diffraction (XRD), and scanning electron microscopy with energy dispersive X-ray spectroscopy (SEM/EDS) analysis.

2.0 Results and Discussion

We will first describe a set of criteria that can be applied to analyze the reaction mechanism and STWS behavior of candidate materials. Next, we will discuss the DFT-predicted behavior of the doped-hercynite and novel aluminates using these criteria. Lastly, we will report the experimental validation of these results in the following order: relative H_2 production capacities of the various aluminates, the phases present during oxidation and reduction, and finally SEM/EDS analysis of the cation distribution in the oxidized or reduced forms of the materials.

2.1 Method for the Computational Evaluations of Possible STWS Cycles

In STWS, the overall enthalpy (286 kJ/mol) and entropy (44.4 J/mol·K) changes of the water splitting reaction must be met, as shown in Equations 7 and 8, and the overall process must be exergonic, as shown in Equation 9.[30] Additionally, if a material is to drive STWS, both its

reduction and oxidation half-reactions must be spontaneous – *i.e.* have a negative Gibbs free energy, as shown in Equations 10 and 11.[13]

$$\Delta H_{STWS} = \Delta H_{TR} + \Delta H_{OX} \geq 286\ kJ/mol \quad (7)$$

$$\Delta S_{STWS} = \Delta S_{TR} + \Delta S_{OX} \geq 44.4\ J/mol \cdot K \quad (8)$$

$$\Delta G_{STWS} = \Delta H_{STWS} - T\Delta S_{STWS} < 0 \quad (9)$$

$$\Delta G_{TR} = \Delta H_{TR} - T_{TR}\Delta S_{TR} < 0 \quad (10)$$

$$\Delta G_{OX} = \Delta H_{OX} - T_{OX}\Delta S_{OX} < 0 \quad (11)$$

Here, STWS indicates the overall reaction cycle, TR indicates the thermal reduction step, and OX indicates the H_2 generating oxidation step. From these equations, several general rules about the half-reactions can be identified. The entropy lost in forming H_2 from H_2O, $\Delta S \approx$ -58 J/mol·K, is too unfavorable for any potential entropy gain from metal oxide re-oxidation to overcome; the maximum entropy gain from oxidation of a candidate material was demonstrated by Meredig *et al.* who showed that none of the 105 metal oxides they assessed gained more than 30 J/mol·K of entropy upon oxidation.[13] Because the oxidation step is entropically unfavorable, the oxidation of the active material must be exothermic ($\Delta H < 0$) with a ΔH greater in magnitude than $T\Delta S$ if the water splitting reaction is to be spontaneous, as shown in Equation 11. Because the enthalpies of both the reduction and oxidation steps together must be greater than the enthalpy of water splitting (Equation 7), the reduction enthalpy must be at least 286 kJ/mol. Through an analogous assessment, candidate materials for CO_2 splitting require a reduction enthalpy of 284 kJ/mol. A material with a reduction enthalpy greater than the energy required for gas splitting releases the excess energy as heat during the exothermic oxidation reaction. Therefore, 286 kJ/mol represents a minimum reduction enthalpy for STWS and based on this requirement, we can assess the viability of candidate STWS materials or reaction mechanisms by comparing their reduction enthalpies to the enthalpy required for water splitting – *i.e.* if the metal oxide reduction enthalpy

is less than the water splitting enthalpy, the suggested material or reaction mechanism is unlikely to drive STWS without the input of external work.

Although a reduced material may store sufficient energy to split water, this does not guarantee that it will do so after reduction at a reasonable operating temperature. As the reduction enthalpy of a particular material increases, the driving force for the water splitting reaction also increases, although the extent of reduction and the associated H_2 production capacity at a given reduction temperature decrease. Therefore, the extent of reduction, if any, must be determined at practical reduction temperatures. This is straightforward when the entropy of reduction is known, for example from thermodynamic tables, and therefore the equilibrium constant can be calculated from the Gibb's Free Energy change and the reduction temperature. If reliable thermodynamic data are not available, this information must be obtained either computationally or experimentally. Otherwise, the direct use of entropy to determine the extent of reduction is not feasible. While the direct use of entropy to predict the extent of reduction is desirable for the sake of completeness, it requires either experimentally evaluating all candidate materials, which defeats the purpose of rapid screening, or calculating the entropy of reduction for each candidate material from first principles. Unfortunately, the accurate calculation of reduction entropies is often challenging. Determining the entropy of a system requires highly accurate partition functions based on the accessible configurational, electronic, and vibrational energy levels. As the complexity of the material structure increases, for example when multiple cations occupy equivalent sites or upon the formation of vacancies, so does the difficulty of computing the configurational component of the partition function due to the combinatorial number of cationic and O-vacancy configurations. Additionally, the effects of local atomic configurations on the phonon modes must also be accounted for because local cationic site

heterogeneity and the introduction of O-vacancies lead to a loss of symmetry at these sites and, thus, more complex phonon calculations to determine the vibrational entropy. Consequently, for complex materials and materials that operate via an O-vacancy mechanism, extra care must be taken to determine the configurational and vibrational factors of the partition function. Furthermore, the electronic contributions to the partition function must be included for materials with band gaps that are small relative to kT, or roughly 0.35 eV at practical STWS temperatures. Therefore, when reliable entropic data are not available and reasonably demanding calculations are unlikely to provide sufficiently accurate results, a new method to estimate the degrees of reduction, and the resulting H_2 generation capacities of candidate materials must be developed.

We propose using a "benchmark" material to predict the H_2 production capacities of candidate materials. We suggest a method in which a material known to drive water splitting, even if very poorly, is chosen as a standard against which to compare readily obtainable reduction enthalpies of candidate materials within a similar STWS class, *i.e.* a similar crystal structure and reaction mechanism. We assume that within a STWS reaction class the reduction entropy of the benchmark (subscript "ben") and candidate (subscript "can") materials are approximately the same ($\Delta S_{ben} \approx \Delta S_{can}$). Therefore, when comparing the relative equilibrium extents of reduction between the two materials the $T\Delta S$ terms cancel, as implied by Equation 12.

$$r_{ben,can}(T) = \frac{e^{\left(\frac{-\Delta G_{can}}{RT}\right)}}{e^{\left(\frac{-\Delta G_{ben}}{RT}\right)}} \approx \frac{e^{\left(\frac{-\Delta H_{can}}{RT}\right)}}{e^{\left(\frac{-\Delta H_{ben}}{RT}\right)}} = e^{\left(\frac{-\Delta\Delta H_{can,ben}}{RT}\right)} \qquad (12)$$

Here, $r_{ben,can}$ is the predicted relative extent of reaction and $\Delta\Delta H_{can,ben}$ is the difference in reduction enthalpies between the candidate and benchmark materials. The thermodynamic quantities (ΔG and ΔH) all refer to the reduction reaction. When $r_{ben,can}<1$ the candidate material is predicted to have a lower H_2 production capacity than the benchmark material. For this

analysis to be valid, the material must possess a reduction energy of at least 286 kJ/mol. Thus, we propose to assess the water splitting ability of materials by a two-stage screening: first, we determine if the material or reaction pathway has sufficient energy to split water. If so, then we compare its ability to drive water splitting to previously characterized materials of a similar class as outlined in Equation 12.

2.2 Computational Evaluation of Possible Aluminate Cycle STWS Materials and Mechanisms

Using the approach described in Section 2.1, we evaluated the abilities of the previously undemonstrated pure hercynite ($FeAl_2O_4$) and cobalt aluminate ($CoAl_2O_4$) cycles to split water in relation to the proven doped-hercynite ($Co_xFe_{1-x}Al_2O_4$) cycle. To do this, we must know the associated reaction mechanisms; therefore, we first determined the reaction mechanism using the minimum reduction energy criteria before predicting the STWS abilities of candidate oxides.

In order to determine the reaction mechanism for a STWS material, the reduction energy for each considered path is calculated and then compared to the minimum reduction energy criteria. This results in three possible cases: 1) none of the analyzed mechanisms has sufficient reduction enthalpy to drive water splitting; 2) only one of the analyzed mechanisms has sufficient reduction enthalpy to drive water splitting; or 3) more than one analyzed reaction mechanism can drive water splitting. The first case is uninteresting as the material is incapable of splitting water by the analyzed mechanisms. In the second case, the mechanism with a reduction enthalpy greater than 286 kJ/mol is the active mechanism. In the third case, all mechanisms with reaction energies sufficient to drive water splitting are potentially active, and their activities are determined by their relative kinetics and thermodynamics at the operating conditions. A comparison of the O-vacancy and stoichiometric mechanisms shows that the O-vacancy

mechanism represents the initial stages of the stoichiometric reaction at a temperature where insufficient thermal energy is available to fully decompose the material into a separate phase. Therefore, at reduction temperatures below that required for phase decomposition, the O-vacancy mechanism would be active and at reduction temperatures above this threshold, the stoichiometric reaction mechanism becomes active. The temperature at which this crossover occurs can be estimated from the stoichiometric reaction reduction enthalpy by determining the temperature at which the Gibbs free energy of the stoichiometric reaction becomes negative and making the approximation that the entropy change of the system is equivalent to the entropy of O_2 formation, i.e. neglecting entropic contributions from the solid phase. These three cases allow us to easily assess the reaction mechanism only knowing the reduction energy.

2.2.1 Thermodynamics and Reaction Mechanism of the Doped-Hercynite STWS Cycle

We calculated the reduction energy of the hercynite stoichiometric reaction to be 175 kJ/mol, as reported in Table 1. The low reduction enthalpy of the stoichiometric mechanism indicates that the stoichiometric doped-hercynite cycle does not possess the reducing power to split water. Additionally, if the reaction forms a single mixed aluminate rather than separate Fe and Co aluminates, the reaction energy is even lower (166 kJ/mol, as shown in Table 1). This indicates that, although the mixed aluminate forms during reduction, as it is lower in energy then separate aluminate phases, it is incapable of splitting water. Therefore, we predict that the stoichiometric reaction mechanism is not the active pathway in the doped-hercynite STWS cycle and another mechanism that is consistent with the demonstrated ability of the doped-hercynite cycle to drive STWS must be active.

The formation of O-vacancies in a doped-hercynite ($Co_{0.5}Fe_{0.5}Al_2O_4$) material is endothermic by at least 384 kJ/mol, as shown in Table 1. This indicates that reduced $Co_{0.5}Fe_{0.5}Al_2O_4$ has sufficient energy to split water and suggests that the doped-hercynite cycle could operate via an O-vacancy mechanism, where the $CoFe_2O_4$ initially reacts with alumina to form $Co_{0.5}Fe_{0.5}Al_2O_4$ and then cycles between $Co_{0.5}Fe_{0.5}Al_2O_4$ and $Co_{0.5}Fe_{0.5}Al_2O_{4-\delta}$.

Table 1: Comparison of the reduction energies of various possible doped-hercynite cycle reaction mechanisms.

Reaction Type	Reduction Reaction		Reduction Energy (kJ/mol)	Water Splitting Capable
Stoichiometric	$CoFe_2O_4 + 3Al_2O_3 \rightarrow CoAl_2O_4 + 2FeAl_2O_4 + ½\ O_2$		175	No
	$CoFe_2O_4 + 3Al_2O_3 \rightarrow 3\ Co_{0.33}Fe_{0.66}Al_2O_4 + ½\ O_2$		166	No
O-vacancy	$Co_{0.5}Fe_{0.5}Al_2O_4 \rightarrow Co_{0.5}\,Fe_{0.5}\,Al_2O_{4-\delta} + \delta/2\ O_2$	**O-neighboring cations[a]**		
		One Fe	573	Yes
		Two Fe	508	Yes
		Three Fe	450	Yes
		Four Fe	384	Yes
		One Co	621	Yes
		Two Co	515	Yes
		Three Co	436	Yes
		Four Co	403	Yes

[a]Number and type of non-Al cations neighboring the O to be removed; the balance of the four O-neighboring cations is composed of Al cations.

As shown in Table 1 and Figure 1a, the predicted O-vacancy formation energies of $Co_{0.5}Fe_{0.5}Al_2O_4$ span a range from 384-621 kJ/mol. The wide range stems from the variation in the local environments of the O atom whose removal generates the O-vacancy and which goes on to form O_2. The geometries of the O-vacancies with different cationic configurations are

shown in Figure 1c. The more Al cations that neighbor an O anion, the more endothermic it is to produce an O-vacancy at that site. O anions in the spinel structure are tetrahedrally coordinated to three octahedrally coordinated cations and one tetrahedrally coordinated cation. In normal spinels, such as $FeAl_2O_4$, $CoAl_2O_4$, and $Co_xFe_{1-x}Al_2O_4$, the Al cations occupy the octahedral sites while the Co and Fe cations occupy the tetrahedral sites. This means that each O atom is nominally coordinated to three Al cations and one Fe or Co cation. However, at the high temperatures necessary for STWS, the cations of normal spinels become less ordered due to entropic driving forces and form structures which are

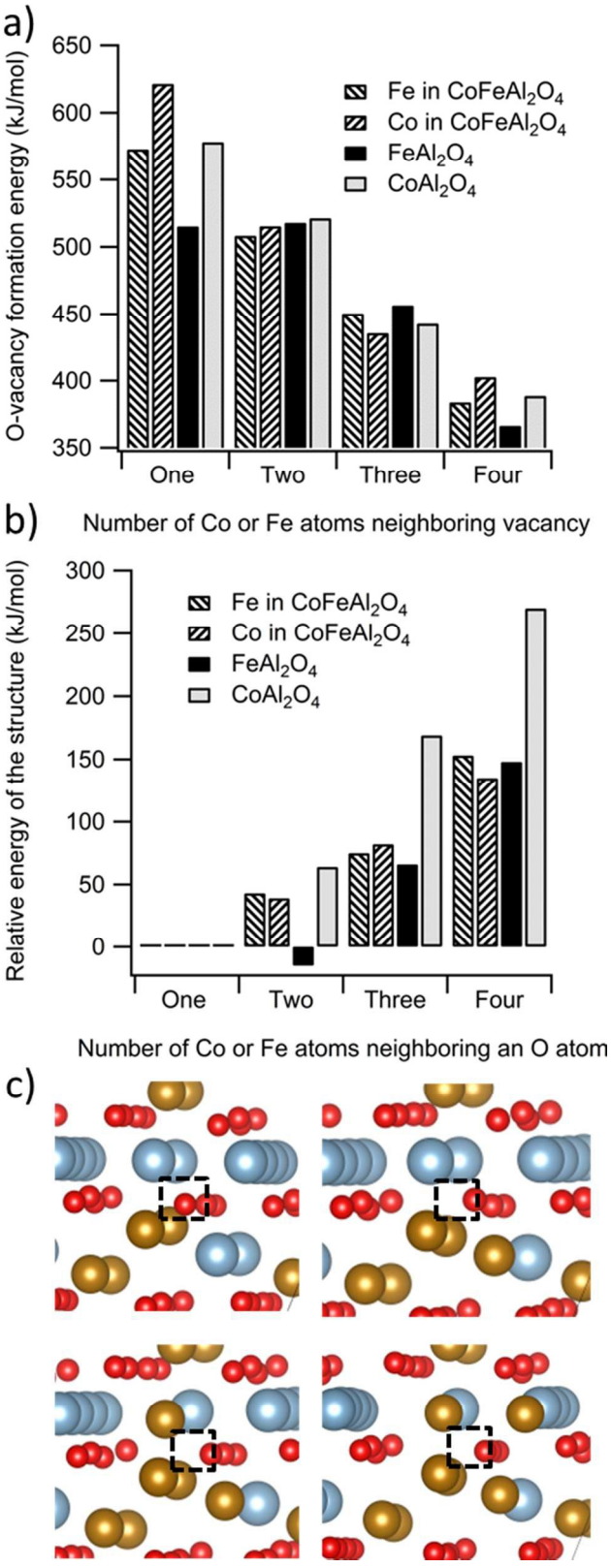

Figure 1: a) Calculated O-vacancy formation energies at sites with varying numbers of Co or Fe nearest neighbors and b) the relative energies of exchanging cations to produce O sites with multiple Co or Fe nearest neighbors. c) The configurations of the ions in the $FeAl_2O_4$ spinel for an O-vacancy with one (top left), two (top right), three (bottom left), and four Fe neighbors (bottom right). The large blue, medium gold and small red spheres represent Al, Fe and O atoms respectively and the black square indicates the location of an O-vacancy.

partly normal and partly inverse.[31] At 1200°C, which is the onset temperature for the doped-hercynite STWS cycle, $FeAl_2O_4$ and $CoAl_2O_4$

are predicted to be 23% and 2% inverted, respectively. These values are in good agreement with previously determined computational values[29] and experimental results (15-20%[32] and ~5%[33]). This suggests that atomic configurations in the doped-hercynite material exist where an O^{2-} anion neighbors more than one Co or Fe cation. Additionally, using the rationale outlined in Equation 12 and described at the beginning of Section 2.2, together with the relative O-vacancy formation energies reported in Table 1 we determine that reduction is most likely to occur at O atoms coordinated to four Co or Fe cations.

When an O is removed from a site where it neighbors three Al cations and one Fe or Co cation, the O-vacancy formation energy is 573 and 621 kJ/mol, respectively. While O-vacancies at these sites certainly have the reducing power to split water, few are likely to exist at achievable STWS temperatures because of the high O-vacancy formation energy. However, as the extent of inversion increases and Al cations neighboring an O anion are exchanged for Co or Fe cations, the O-vacancy formation energy decreases down to 384 and 403 kJ/mol for an O anion neighboring four Fe and Co cations, respectively, as shown in Table 1 and Figure 1. This suggests that the O sites that neighbor multiple Fe and Co cations are the likely sites for O-vacancy formation, and, therefore, are the likely sites for driving STWS because they both exist in significant quantities and possess the enthalpy required to split H_2O.

The preference for O-vacancies to neighbor multiple Co and Fe cations stems from the relative strengths of the O-cation bonds and the reducibility of the cations involved. It is well known that O forms a stronger bond to Al ($\Delta H_{f\ Al2O3}$ = -558 kJ/mol per Al-O bond), than to Fe ($\Delta H_{f\ FeO}$ = -272 kJ/mol) or Co ($\Delta H_{f\ CoO}$ = -237 kJ/mol).[34] The formation of O-vacancies neighboring more than one Fe and Co cation breaks fewer strong O-Al bonds, thus lowering the O-vacancy formation energy. Additionally, when reduction occurs, the individual O^{2-} anions

oxidize and donate two electrons to the cations in the system. As the number of Al cations neighboring the O-vacancy decreases, more Fe or Co cations are available to accept this charge, and, therefore, fewer Al cations reduce to an unfavorable oxidation state of less than +3, as shown in Table 2. Furthermore, when more Co and Fe cations neighbor the formed O-vacancy, the charge transferred to any individual cation generally decreases. This further lowers the O-vacancy formation energy because the Co^{2+} and Fe^{2+} cations do not deviate as much from their stable +2 oxidation state to their less stable +1 oxidation states. Overall, these factors lower the energetic cost of O-vacancy formation at sites with multiple Co or Fe neighbors while still providing sufficient energy to split water. Therefore, it is likely that these sites are active in doped-hercynite STWS. These results suggest that the Co and Fe cations are the active cations in the doped-hercynite cycle and that Al cations are mostly inert but stabilize the spinel structure as the material reduces.

The formation of an oxygen vacancy in doped-hercynite causes the local structure to contract with the lattice constants of our supercell models of the vacancies shrinking by 0.028Å (0.24%) and 0.022 Å (0.19%) for the cases of an O-vacancy with four Fe and four Co nearest neighbors, respectively. The Fe-Fe distances of the O-vacancy with four Fe cation nearest neighbors decrease dramatically; the average tetrahedral Fe to octahedral Fe distance shrinks from 3.46 Å to 2.96 Å, while the average octahedral Fe to octahedral Fe distance shrinks from 2.84 Å to 2.68 Å. Although the Fe-Fe distances decrease, the Fe-O bonds elongate slightly with the average distances between the tetrahedral and octahedral Fe cations neighboring the O-vacancy to their neighboring O atoms increasing by 0.09 and 0.03Å, respectively. Overall, the relaxation of the cations towards the O-vacancy compresses the lattice. We find similar behavior for the case of forming an O-vacancy with four nearest neighbor Co cations. The contraction of the hercynite

material upon O-vacancy formation is noteworthy because this is in contrast to O-vacancy formation in ceria systems which causes a lattice expansion.[35] Our calculations that predict that the O-vacancy mechanism is active in hercynite also predict an associated lattice contraction and expansion upon reduction and oxidation, which could be measured by HT-XRD.

Table 2: The reduction energy of spinel aluminates by stoichiometric and O-vacancy mechanisms

Stoichiometric Reaction						
Reduction Reaction				**Reduction energy** (kJ/mol)		
$CoFe_2O_4 + 3Al_2O_3 \rightarrow 3Co_{0.33}Fe_{0.66}Al_2O_4 + ½ O_2$				166		
$Fe_3O_4 + 3Al_2O_3 \rightarrow 3FeAl_2O_4 + ½ O_2$				182		
$Co_3O_4 + 3Al_2O_3 \rightarrow 3CoAl_2O_4 + ½ O_2$				101		
O-Vacancy Reaction						
Spinel stoichiometry	**Type and number of neighboring Fe or Co cations**	**Relative energy of structure** (kJ/mol)	**Reduction energy** (kJ/mol)	**Average change in oxidation after O-vacancy formation**		
				tetrahedral neighbor	Al octahedral neighbors	Fe/Co octahedral neighbors
$Co_{0.5}Fe_{0.5}Al_2O_4$	One Fe	-	573	1.08	0.13	-
	Two Fe	43	508	0.64	0.17	0.46
	Three Fe	75	450	0.49	0.00	0.50
	Four Fe	153	384	0.50	-	0.30
	One Co	-	621	0.77	0.11	-
	Two Co	39	515	0.58	0.12	0.49
	Three Co	82	436	0.34	0.00	0.49
	Four Co	135	403	0.34	-	0.32
$FeAl_2O_4$	One Fe	-	515	0.85	0.20	-
	Two Fe	-15	518	0.65	0.21	0.38
	Three Fe	66	457	0.54	0.00	0.44
	Four Fe	148	366	0.48	-	0.32
$CoAl_2O_4$	One Co	-	578	0.80	0.18	-
	Two Co	64	521	0.54	0.00	0.78
	Three Co	169	443	0.57	0.13	0.30

	Four Co	270	389	0.42	-	0.31

3.2.2 Predicting the STWS ability of Un-doped Fe- and Co-Aluminate

With an understanding of the mechanism of the doped hercynite cycle in hand, we investigated the ability of un-doped $FeAl_2O_4$ and $CoAl_2O_4$ to drive STWS by calculating the reduction enthalpy for both the stoichiometric and O-vacancy formation reaction mechanisms; the results are shown in Table 2. In a stoichiometric reaction, analogous to that proposed for the hercynite cycle, Fe_3O_4 or Co_3O_4 reacts with Al_2O_3 to form the relevant aluminates upon reduction, *i.e.* $FeAl_2O_4$ or $CoAl_2O_4$, and subsequently oxidizes back to separate phases when splitting water.[20] These reaction mechanisms are shown in Equations 13 and 14 in which M is either Fe or Co. We calculate that the reduction energy for the stoichiometric Fe- and Co-aluminate cycles are 182 and 101 kJ/mol, respectively; therefore, these cycles are not capable of splitting water, in accordance with the thermodynamic argument based on the minimum reduction energy to split water.

$$M_3O_4 + 3Al_2O_3 \rightarrow 3MAl_2O_4 + \frac{1}{2}O_2 \quad (13)$$

$$3MAl_2O_4 + H_2O \rightarrow M_3O_4 + 3Al_2O_3 + H_2 \quad (14)$$

We calculate that O-vacancy formation energies in $FeAl_2O_4$ and $CoAl_2O_4$ range from 366 to 578 kJ/mol depending on the O-nearest neighbor arrangement, as shown in Table 2. This suggests that $FeAl_2O_4$ and $CoAl_2O_4$ are thermodynamically capable of driving water splitting via an O-vacancy mechanism. As we found for the doped-hercynite material, the lowest O-vacancy formation energies occur when the O-vacancy neighbors four Fe or Co cations. This is once again ascribable to the relative preference of Al cations over the Fe and Co cations to be fully

coordinated to O atoms, as described in Section 2.2.1. Additionally, calculations predict that reduction is accompanied by a lattice contraction of 0.036 Å (0.30%) and 0.044 Å (0.38%) for $FeAl_2O_4$ and $CoAl_2O_4$ respectively, in good agreement with our DFT calculated lattice changes.

Although the O-vacancy formation energies of the various aluminate spinels are similar at a given number of Fe or Co nearest neighbors, as shown in Figure 1, the O-vacancy formation energies of $FeAl_2O_4$ are slightly lower than $Co_{0.5}Fe_{0.5}Al_2O_4$ and $CoAl_2O_4$. This difference is 15 kJ/mol and 19 kJ/mol, as averaged over the four possible O-nearest neighbor configurations, and can be up to 18 and 23 kJ/mol when four Fe or Co cations neighbor the O-vacancy, respectively. This indicates that $FeAl_2O_4$ is likely to form more O-vacancies than $Co_{0.5}Fe_{0.5}Al_2O_4$ and $CoAl_2O_4$ under similar reducing conditions. Additionally, the energy to exchange an Al cation at an octahedral site with a tetrahedrally coordinated Co or Fe cation is not constant across the aluminates. It is more energetically favorable to form an O atom coordinated to four Fe or Co cations in $FeAl_2O_4$ and $Co_{0.5}Fe_{0.5}Al_2O_4$ than in $CoAl_2O_4$ by roughly 120 kJ/mol, as shown in Table 2 and Figure 1b. This is consistent with the experimental inversion parameters of 0.15-0.20[32] and 0.05[33] for $FeAl_2O_4$ and $CoAl_2O_4$, respectively. This predicts that more active sites exist in $FeAl_2O_4$ and $Co_{0.5}Fe_{0.5}Al_2O_4$ than in $CoAl_2O_4$. For example, at 1500°C for every oxygen site with four Co or Fe nearest neighbors in $FeAl_2O_4$, roughly 0.7 and 2×10^{-4} such sites exist in $Co_{0.5}Fe_{0.5}Al_2O_4$ (four Fe cations as these have lower O-vacancy formation energies) and $CoAl_2O_4$, respectively, based on Equation 12.

2.2.3 Predicted Relative H_2 Production Capacities of Fe- and Co-Aluminates

Using the reaction energies described in Sections 2.2.1 and 2.2.2, and the method outlined in Section 2.1, we can make predictions of the relative H_2 production capacities and

potential mechanisms of STWS driven by $Co_{0.5}Fe_{0.5}Al_2O_4$, $FeAl_2O_4$, and $CoAl_2O_4$. First, we predicted that Fe- and Co-based aluminates operate via an O-vacancy mechanism rather than a stoichiometric one. For the materials investigated here, the O-vacancies have sufficient energy to drive water splitting. This is evidenced by the O-vacancy formation energies which exceed the threshold required to split water, whereas the stoichiometric reduction energies are less than 286 kJ/mol.

Second, we predict that, after reduction at 1500°C, the aluminates possess a H_2 production capacity ratio of roughly 1 to 0.7 to 2×10^{-4} for $FeAl_2O_4$, $Co_{0.5}Fe_{0.5}Al_2O_4$, and $CoAl_2O_4$, respectively. The predicted ratio of H_2 production capacities is based on the relative number of sites within each material with four Co or Fe neighbors, as calculated using Equation 12. This is because each of the materials has comparable O-vacancy formation energies at sites with the same number of Co or Fe neighbors, which suggests that O-vacancies will form at these sites in similar proportion, but that the number of active sites that each of the materials has differs, as discussed in Section 2.2.2. Therefore, the material which has the largest number of STWS active sites, *i.e.* O-sites with four Co or Fe neighbors, should produce the most H_2.

Finally, if the predicted enthalpic minimum for water splitting does not exist, we predict based on Equation 12 that the relative H_2 production capacities of the aluminates would be $CoAl_2O_4$ > $Co_{0.5}Fe_{0.5}Al_2O_4$ > $FeAl_2O_4$ in ratios of 1 to 0.012 to 0.004 if a hypothetical stoichiometric reaction was active. This assumes that all of the reduced material is capable of splitting water regardless of the reduction enthalpy. The predicted relative H_2 production capacity of these materials operating via a stoichiometric reaction mechanism is the opposite of the predicted H_2 production capacity of the materials operating via an O-vacancy mechanism. This suggests that the operational mechanism, the validity of the thermodynamic arguments, and

STWS material screening criteria outlined in Section 2.2.1 can be validated by experimentally determining the relative H_2 production capacities of the three aluminates and comparing their relative H_2 production capacities.

2.3 H_2 Generation by Fe- and Co-Aluminates

We determined the STWS H_2 production capacities of $CoAl_2O_4$, $FeAl_2O_4$, and $Co_{0.4}Fe_{0.6}Al_2O_4$ in a SFR by cycling the materials near-isothermally between 1500°C and 1350°C. The results are shown in Figure 2a. Overall, the H_2 production capacities of the aluminate materials are $FeAl_2O_4$ (510±40 µmol H_2/g) > $Co_{0.5}Fe_{0.5}Al_2O_4$ (310±30 µmol H_2/g) > $CoAl_2O_4$ (6±10 µmol H_2/g). Because no statistically significant quantity of H_2 was produced by the $CoAl_2O_4$, (6±10 µmol H_2/g is statistically indistinguishable from 0 µmol H_2/g at a 95% confidence level) we will refer to its production as 0 µmol H_2/g for the rest of this discussion. The H_2 production ratios of the aluminates are 1 to 0.6 to 0 for $FeAl_2O_4$, $Co_{0.5}Fe_{0.5}Al_2O_4$, and $CoAl_2O_4$, respectively. This agrees with the computationally predicted relative H_2 production capacities for the aluminates operating via an O-vacancy mechanism of 1 to 0.7 to 2×10^{-4} for $FeAl_2O_4$, $Co_{0.5}Fe_{0.5}Al_2O_4$, and $CoAl_2O_4$,

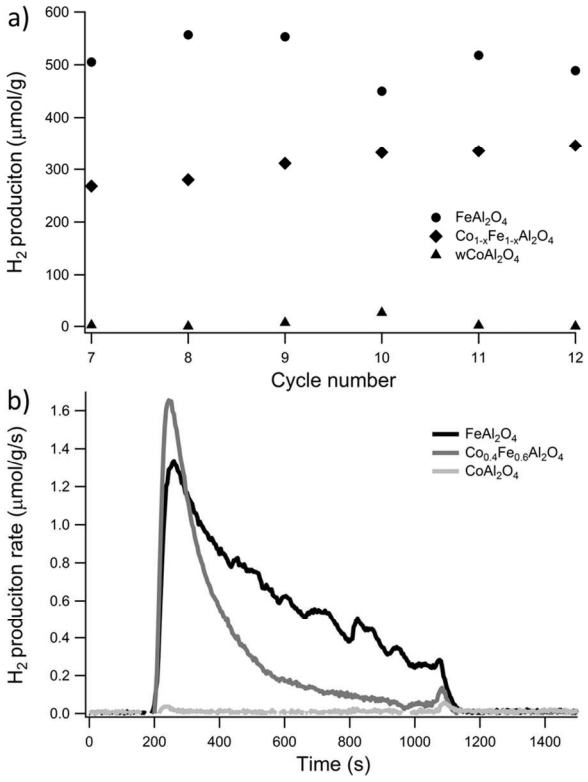

Figure 2: a) The H_2 production capacities of $FeAl_2O_4$, $Co_{0.4}Fe_{0.6}Al_2O_4$, and $CoAl_2O_4$ during near-isothermal water splitting cycling at 1500/1350°C over multiple cycles. The $CoAl_2O_4$ cycles are labled as cycles 7-12 but represent cycles 1-6 so they can be displayed on the same horizontal axis. b) The rate of H_2 production of $FeAl_2O_4$, $Co_{0.4}Fe_{0.6}Al_2O_4$, and $CoAl_2O_4$ for a typical cycle (the ninth cycle for $FeAl_2O_4$ and $Co_{0.4}Fe_{0.6}Al_2O_4$, and the third cycle for $CoAl_2O_4$).

respectively. This suggests that the screening parameters for STWS viability and reaction mechanism are valid.

The peak H_2 production rates are 1.64±0.02 and 1.32±0.07 μmol H_2/s·g for $Co_{0.4}Fe_{0.6}Al_2O_4$ and $FeAl_2O_4$, respectively, as shown for represented H_2 production traces in Fig. 2b. While $Co_{0.4}Fe_{0.6}Al_2O_4$ produces less H_2 than $FeAl_2O_4$, the presence of Co cations increases the rate of the oxidation reaction. This could occur either by catalyzing the surface water splitting reaction or increasing the rate of O^{2-} cation diffusion through the bulk material. Based on previous work which indicated that the doped-hercynite cycle oxidation reaction is surface limited,[36] we hypothesize that the presence of Co cations increases the rate of surface H_2O splitting and/or H_2 formation reactions.

Overall, these experimental findings demonstrate that, after reduction at 1500°C, both doped- and un-doped-hercynite ($FeAl_2O_4$) are capable of driving STWS while $CoAl_2O_4$ is not. This is consistent with the computational predictions that doped- and un-doped-hercynite both operate via an O-vacancy STWS mechanism and that the thermodynamic argument suggesting a reduction enthalpy of ≥286 kJ/mol is valid. Additionally, this shows that the reduction enthalpy requirement is a valid metric for assessing candidate STWS materials and for determining which mechanism is active. Lastly, by comparing the relative number of active sites available at a reduction temperature and the O-vacancy formation energies of novel materials, the relative H_2 production capacities can be predicted.

2.4 Analysis of the Phases Present during Doped-Hercynite STWS

We isothermally cycled ALD-produced doped-hercynite material in a HT-XRD at 1400 °C under He and CO_2 atmospheres to determine the phases present during reduction and oxidation to validate the computationally determined reaction mechanism. The characteristic peaks of an aluminate spinel and alumina were present during both the reduction and oxidation steps, but a $CoFe_2O_4$ signal was absent from both steps; as shown in Figure 3. The lack of a $CoFe_2O_4$ peak in the HT-XRD pattern indicates that this phase does not form nor decompose as the material cycles between the reduced and oxidized states. Additionally, the intensity of the Al_2O_3 peak does not change significantly over the course of cycling. This indicates that no significant change occurs in the quantity of Al_2O_3 present during redox cycling, which would be expected if a stoichiometric reaction mechanism were active. The XRD pattern of the specimen measured at room temperature after redox cycling at 1400 °C showed that the same

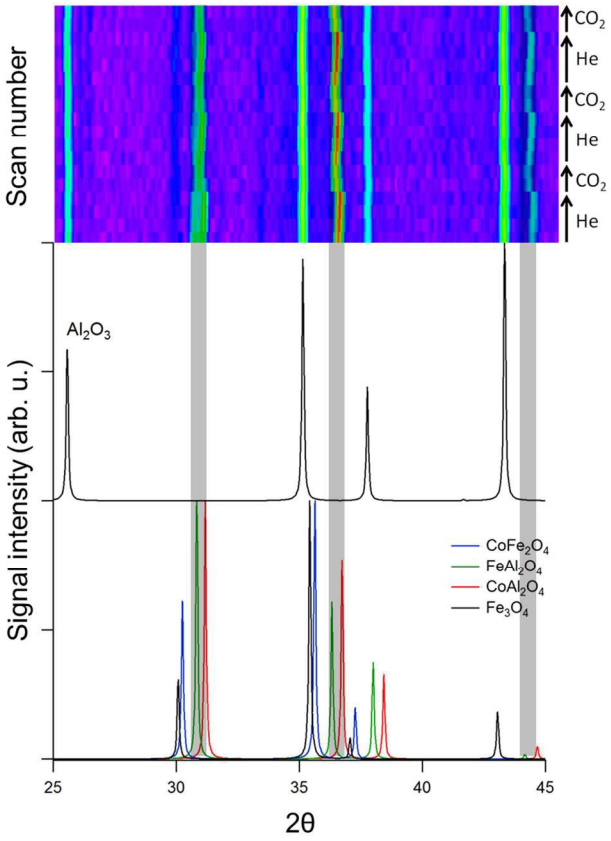

Figure 3: Top: HT-XRD of doped-hercynite material as it undergoes several cycles of CO_2 splitting at 1400 °C. The horizontal axis displays 2θ while the vertical axis represents time. Each row of pixels is the XRD scan at a given time point. The scans progress with time from the bottom of the graph to the top, as indicated by the arrows on the right hand side of the graph. The intensity of the XRD spectrum at each 2θ is indicated by the color of the pixel where warm colors (red, bright green, and blue) indicate a more intense XRD signal and cool colors (purple and dark blue) represent a low signal. The atmosphere present in the HT-XRD during any given XRD scan is indicated on the right side of the plot, where the presence of He and CO_2 drive reduction and oxidation, respectively. The bottom panel shows the XRD patterns of Al_2O_3 and various spinels. Gray bars have been added to aid the eye in aligning the XRD peaks of the three graphs. The Al_2O_3 peaks in the HT-XRD scan are aligned to the room temperature Al_2O_3 XRD peaks for ease of comparison.

phases are present as those observed during high temperature cycling as well as at room temperature prior to cycling. This verifies that irreversible changes to the structure of the doped-hercynite did not occur under cycling conditions. Therefore, we conclude that the doped-hercynite cycle does not likely operate via a stoichiometric reaction mechanism in agreement with our computational predictions that the stoichiometric reaction does not have sufficient reducing power to split water or CO_2.

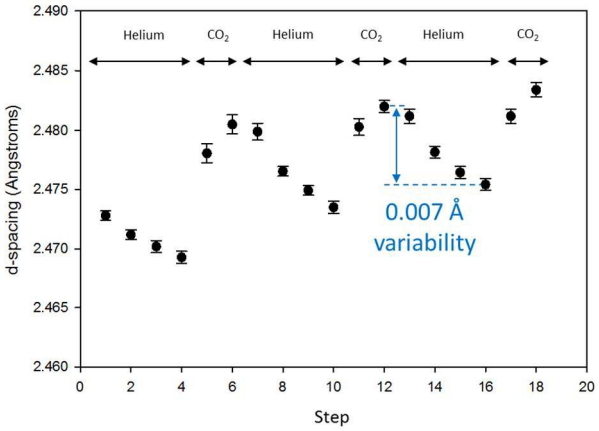

Figure 4: The changes in the (311) d-spacing of the doped-hercynite material as it undergoes isothermal reduction and CO_2 splitting oxidation at 1400 °C. The reduction and oxidation steps are indicated by the atmosphere in the system shown at the top of the graph, where helium and CO_2 are present during the reduction and oxidation steps respectively.

The aluminate spinel peak also provides information about the reaction mechanism. The location of this observed peak is close to the characteristic 2θ of both $CoAl_2O_4$ and $FeAl_2O_4$. Because the characteristic peaks of these spinels exhibit only a small difference in 2θ and the width of the observed XRD peak is large, it is difficult to ascertain whether a single mixed $Co_xFe_{1-x}Al_2O_4$ phase or separate $CoAl_2O_4$ and $FeAl_2O_4$ phases are present. However, our calculations predict that at equilibrium a mixed phase exists due to its lower energy. As Figure 3 shows, the aluminate peaks shift to higher and lower 2θ positions as the material undergoes reduction and oxidation, respectively, with a measured d-spacing change for hercynite (311), Figure 4, of roughly 0.007 Å over a redox cycle indicating the extent that the material contracts during reduction and expands during oxidation. The d-spacing changes (Δd) on reduction and oxidation are consistent with our DFT predictions of lattice contraction upon O-vacancy formation and expansion upon re-oxidation. In order to discount the possibility of Δd being caused by thermal expansion/contraction (i.e., changing sample temperature due to the difference

in heat capacity/conductivity of He versus CO_2), an identical experiment was performed using a Pt/Al_2O_3 standard in place of hercynite (Figure SI.3a). Neither the Pt, nor the Al_2O_3 are expected to exhibit any chemical reactivity under these conditions, and the thermal expansion coefficients of Al_2O_3 and hercynite are of the same sign and of similar magnitude (<8% difference)[37, 38]. The Al_2O_3 (104) Δd changes in the opposite direction to hercynite (311), and at a much lower magnitude, indicating that the hercynite (311) changes are due to chemical, not thermal changes. Furthermore, the excess Al_2O_3 in the hercynite specimen showed comparable behavior to the Pt/Al_2O_3 standard (Figure SI.3b), adding support to our conclusion that Al_2O_3 is not an active participant in the redox cycling.

A further observation which can be made of the data in Figure 4 is the steady decrease in hercynite d(311) during each 50 minute helium soak (reduction step), which reflects the finite kinetics of oxygen vacancy formation in such systems, whereas upon exposure to CO_2 the d-spacing increases rapidly showing that re-oxidation of reduced hercynite is a more rapid process.

Overall, the constant presence of the aluminate phase and the lack of $CoFe_2O_4$ suggest that a stoichiometric reaction between $CoFe_2O_4$ and Al_2O_3 is not occurring. Additionally, the expansion and contraction in the aluminate phase during oxidation and reduction is consistent with the computationally predicted O-vacancy mechanism. These findings are in agreement with the thermodynamic analysis, DFT, and SFR results, leading further credence to the validity of the minimum reduction energy screening criterion.

2.5 Investigation of Phase Segregation During Doped-Hercynite STWS

We determined phase and cation segregation (Co and Fe cations away from Al) after reduction or oxidation using SEM/EDS analysis on FIB-milled doped-hercynite samples. The

results are shown in SI Figure SI.4. The EDS maps of the cation distributions in the bulk materials show that there is no significant segregation of any of the cations in either the reduced or oxidized states, as is shown in SI Figures SI.4c-j. Therefore, it is unlikely that a major phase change occurs between the oxidation and reduction steps. This is in contrast to the cation distribution of $CoFe_2O_4$ deposited on ZrO_2 which does not exhibit significant mixing of the $CoFe_2O_4$ and ZrO_2 phases, as shown in the SEM and EDS maps of SI Figures SI.4k-p.[39] The EDS results agree with the computational, SFR, and HT-XRD experimental results that the hercynite reaction is not a stoichiometric reaction.

3.0 Conclusions

In this contribution, we developed a method for evaluating the ability of complex metal oxides to drive STWS and the reaction mechanism by which they operate. We have shown that DFT accurately predicts the redox properties and thus STWS behavior of spinels based on their cationic exchange and reduction enthalpies. This is likely extendable to other crystal structures. Overall, materials or reaction paths with lower reduction enthalpies and/or more active sites produce the most H_2 at a given temperature as long as they satisfy the thermodynamic condition of possessing a reduction enthalpy required to split water. DFT calculations show that Fe- and Co-aluminates operating via a stoichiometric reaction mechanism have insufficient reducing power to split water, having reduction enthalpies of 101, 182, and 166 kJ/mol for $CoAl_2O_4$, $FeAl_2O_4$, and $Co_{0.5}Fe_{0.5}Al_2O_4$, respectively. However, our DFT calculations predict that these materials can drive STWS via an O-vacancy mechanism instead, where $CoAl_2O_4$, $FeAl_2O_4$, and $Co_{0.5}Fe_{0.5}Al_2O_4$ have minimum reduction enthalpies of 389, 366, and 383 kJ/mol, respectively, when the O-vacancy neighbors four Fe or Co cations. O-vacancies preferentially occupy sites

neighboring multiple Fe or Co cations, suggesting that the Co and Fe cations are the active cations and Al cations stabilize the spinel phase. However, due to the relative formation energies of these sites, we predict relative H_2 production capacities of 1 to 0.7 to 2×10^{-4} for $FeAl_2O_4$, $Co_{0.5}Fe_{0.5}Al_2O_4$, and $CoAl_2O_4$, respectively. We also determined relative H_2 production capacities of 1 to 0.6 to 0 for $FeAl_2O_4$, $Co_{0.5}Fe_{0.5}Al_2O_4$, and $CoAl_2O_4$ based on their H_2 production capacities of 510±40, 310±30, and 6±10 μmol H_2/g measured using SFR water splitting experiments. This validates the computational predictions of the aluminates to drive STWS behavior and confirmed that the O-vacancy mechanism we predicted using DFT is indeed correct. Additionally, our results suggest that $FeAl_2O_4$, which had not yet been experimentally demonstrated, may be a better STWS material than $Co_{0.5}Fe_{0.5}Al_2O_4$.

These predictions were confirmed using HT-XRD and SEM/EDS analysis. Our HT-XRD analysis shows that during doped-hercynite cycling no $CoFe_2O_4$ was present, but the aluminate spinel persists throughout both reduction and oxidation. Additionally, the expansion and contraction of $Co_xFe_{1-x}Al_2O_4$ during oxidation and reduction suggests that vacancies are forming in the spinel material, further validating the computational assessment. EDS mapping shows that the Co, Fe, and Al cations are well mixed after both reduction and oxidation, further confirming our predictive analysis. Overall, this work demonstrates a simple approach to accurately predict the STWS ability of novel materials by employing a 286 kJ/mol reduction enthalpy lower bound and comparing their extents of reduction (based on their relative reduction enthalpies) to a benchmark material. We show this through the prediction and verification that the doped-hercynite cycle operates via an O-vacancy mechanism rather than a stoichiometric mechanism, and demonstrates a new STWS material. The ability to predict the STWS ability of complex metal oxides for which experimental thermodynamic data do not exist will enable rapid

screening and development of more efficient novel STWS materials and bring the promise of efficient STWS closer to fruition.

4.0 Methods

We will briefly describe the methods we employed, for a more detailed description see the SI.

4.1 Computational Methods

We performed plane wave periodic boundary condition DFT simulations using the Vienna Ab-initio Simulation Package (VASP).[40, 41] Calculations employed the Perdew-Burke-Ernzerhof (PBE) generalized gradient approximation (GGA) exchange and correlation functional[42] coupled with projector augmented wave (PAW) pseudopotentials.[43] Hubbard on-site correction terms[44] of U_{eff} = 3 and 2 eV on the Fe and Co d-electrons, respectively, were included in the calculations because the GGA functional alone does not adequately describe the electron correlation in these systems. These values of U have been shown to accurately model the electronic structure of Fe and Co aluminates.[45] Bader charge analysis was conducted using software from the Henkelman group.[46, 47] The 112 atom spinel supercell is composed of eight primitive cells in a 2×2×2 arrangement, as shown in SI Figure SI1. We chose a random distribution of cations for inverse spinels where multiple elements reside on the A sites. The calculated relative energies of the inverse and normal configurations of the spinels considered in this work are reported in SI Table SI 1. Several spin configurations were attempted for each spinel, including ferromagnetic and multiple anti-ferromagnetic structures. The relative energies of the various spin configurations

are also shown in SI Table SI1. The lowest energy spin configurations were used in calculating reaction energies.

4.2 Materials Preparation

Doped-hercynite was produced by both atomic layer deposition (ALD) and a modified Pechini (citrate gel) method.[48] All ALD depositions were performed in a vibrating fluidized bed reactor described elsewhere.[27, 49, 50] Thin films of Al_2O_3 were deposited on Cavilink^{TM} polymer supports, followed by deposition of $CoFe_2O_4$. This produced material that is 19.8% $CoFe_2O_4$ with the balance being alumina. This results in a material that is 47% active on a mass basis where the active material is defined as the percent of the total material which is capable of forming $Co_xFe_{1-x}Al_2O_4$. The ALD produced material was used in the HT-XRD and SEM/EDS experiments reported herein. Citrate gel fabrication was used to produce $FeAl_2O_4$ and $(Co_{0.4}Fe_{0.6})_{1.2}Al_{1.8}O_4$ for use in the H_2O splitting stagnation flow reactor experiments. ICP-OES determined that $FeAl_2O_4$ and $(Co_{0.4}Fe_{0.6})_{1.2}Al_{1.8}O_4$ had compositions of $Fe_{1.19}Al_{1.81}O_4$ and $(Co_{0.41}Fe_{0.59}Al_2O_4 + 0.105\ Al_2O_3)$, respectively. $CoAl_2O_4$ (≥99% purity) was purchased from Sigma Aldrich. XRD analysis confirms that we formed the desired spinel phases for the materials fabricated by the Pechini method, as shown in SI Figure SI.2. For additional details of the fabrication methods employed, see the SI Section SI.2. Throughout this work we consider any excess Al_2O_3 to be a segregated inert phase; for a justification of this assumption see SI Section SI.4. While two methods of material preparation were used, we do not directly compare results obtained from the different fabrication methods.

4.3 Experimental Methods

We used three different experimental approaches to validate the computational results: H_2O splitting experiments carried out in a stagnation flow reactor, high temperature XRD analysis, and SEM/EDS analysis.

4.3.1 Method for Determining H_2 Production Capacity of Aluminates

We determined the H_2 production capacity of the doped-hercynite material and the $CoAl_2O_4$ and $FeAl_2O_4$ materials in an in-house fabricated stagnation flow reactor coupled to a Stanford Research QMS200 mass spectrometer with a capillary sampling port to measure the H_2 generation.[7] The active materials were allowed to reduce for 60 min at 1500°C and a total pressure of 760 Torr; a 300 sccm flowrate of He swept the generated O_2 out of the reactor. Oxidation occurred for 15 min at 1350°C and a 760 Torr total pressure in a 50% H_2O/50% He environment with a total gas flow rate of 400 sccm. Steam was fed using an RSIRC steam feeder. Blank runs with no active material present in the reactor were conducted and the H_2 production from heterolytic water splitting was subtracted from the sample runs. The $FeAl_2O_4$ and $Co_{0.4}Fe_{0.6}Al_2O_4$ materials were cycled 12 times while the $CoAl_2O_4$ was only cycled 6 times because no STWS activity was observed. The first six cycles of $FeAl_2O_4$ and $Co_{0.4}Fe_{0.6}Al_2O_4$ are not reported as these cycles are not representative of the long term material behavior due to material sintering in the initial cycles.[51] Average H_2 production capacity confidence intervals are reported for the last six cycles at a 95% confidence level.

4.3.2 Method for Determining Solid Phases during Doped-Hercynite Driven STWS

We performed high temperature X-ray diffraction (HT-XRD) experiments to determine the solid species present during isothermal doped-hercynite CO_2 splitting. CO_2 was employed as the oxidizing gas instead of water to prevent condensation within the HT-XRD and because CO_2 and

H_2O behave similarly as oxidants in solar redox cycles. The XRD patterns were measured using a Scintag PAD X diffractometer (Thermo Electron Inc.; Waltham, MA). See the Supporting Information for further details about the HT-XRD. *In situ* HT-XRD experiments were conducted at atmospheric pressure under gas flow rates of 150 sccm. Experiments typically involved purging the reaction chamber with He, then ramping the temperature to 1400 °C which was held for three isothermal reduction and oxidation cycles. During each cycle the material was allowed to reduce under He for 50 min, and then oxidize under CO_2 for 26 min.

4.3.3 Method for Determining Phase and Cation Segregation

In addition to XRD analysis, we conducted SEM/EDS analysis to determine if separate spinel and alumina phases form or if a single phase is present after both reduction and oxidation. Additionally, this analysis enabled us to determine if the Fe, Co, and Al cations remained well mixed or were segregating within a single phase during cycling. This study used ALD-produced doped-hercynite material which had been pre-cycled over 200 times. Both a reduced and oxidized sample were produced in the SFR, and then analyzed via SEM/EDS. We produced the reduced sample by heating the doped-hercynite material to 1450°C and allowing it to reduce under a 300 sccm He flow for four hours to ensure the material reached equilibrium. The active material was subsequently cooled to room temperature under inert flow. The oxidized sample was produced by first reducing it, as described above, and then oxidizing the reduced material for four hours at 1450°C under a CO_2 atmosphere before the sample was cooled to room temperature in the oxidizing environment. Surface material was removed from the samples via focused ion beam (FIB) milling to expose cross sections of bulk material. This was then used to determine the distribution of cations within the material. FIB milling was performed using a dual beam FEI Nova 600 Nanolab with a Ga beam for ablation. The milled samples were Au coated

to minimize sample charging. SEM/EDS analysis was conducted using a JEOL JSM-6480LV scanning electron microscope.

5.0 Acknowledgements

The authors gratefully acknowledge the National Science Foundation and the U.S. Department of Energy for supporting this research. The work was completed through the National Science Foundation via Grants CBET-0966201 and CBET-1433521 and by the U.S. Department of Energy, Office of Energy Efficiency and Renewable Energy, Fuel Cell Technologies Office under Award Number DE-EE0006671. This work was a collaboration between the University of Colorado Boulder and Sandia National Laboratories. Sandia is a multi-program laboratory operated by Sandia Corporation, a Lockheed Martin Company, for the U.S. Department of Energy's National Nuclear Security Administration under Contract DE-AC04-94AL85000. CLM and BDE would like to thank the Department of Education for support through a Renewable and Sustainable Energy Graduate Assistance in Areas of National Need (GAANN) Fellowship. This work utilized the Janus supercomputer, which is supported by the NSF (award number CNS-0821794) and the University of Colorado Boulder. The Janus supercomputer is a joint effort of the University of Colorado Boulder, the University of Colorado Denver and the National Center for Atmospheric Research. We would like to thank A.H. McDaniel for his valuable suggestions and contributions to this work. We thank M.A. Rodriguez and J. Griego (Sandia National Laboratories) for assistance with the HT-XRD measurements.

[†]Current address: Department of Mechanical and Process Engineering, ETH Zürich, Zürich, 8092, Switzerland

6.0 Bibliography

1. E. A. Fletcher and R. L. Moen, *Science*, 1977, **197**, 1050-1056.
2. A. Steinfeld, *Solar Energy*, 2005, **78**, 603-615.
3. J. E. Miller, A. H. McDaniel and M. D. Allendorf, *Advanced Energy Materials*, 2014, **4**.
4. T. Nakamura, *Solar Energy*, 1977, **19**, 467-475.
5. I. Ermanoski, J. Miller and M. Allendorf, *Physical Chemistry Chemical Physics*, 2014, **16**, 8418-8427.
6. J. R. Scheffe and A. Steinfeld, *Materials Today*, 2014, **17**, 341-348.
7. C. L. Muhich, B. W. Evanko, K. C. Weston, P. Lichty, X. Liang, J. Martinek, C. B. Musgrave and A. W. Weimer, *Science*, 2013, **341**, 540-542.
8. C. Perkins and A. W. Weimer, *AIChE Journal*, 2009, **55**, 286-293.
9. C. L. Muhich, B. D. Ehrhart, I. Al Shankiti, B. J. Ward, C. B. Musgrave and A. W. Weimer, *WIREs Energy and Environment*, 2015, **3**.
10. C. Perkins and A. W. Weimer, *International Journal of Hydrogen Energy*, 2004, **29**, 1587-1599.
11. S. Abanades, P. Charvin, G. Flamant and P. Neveu, *Energy*, 2006, **31**, 2805-2822.
12. T. Kodama, *Progress in Energy and Combustion Science*, 2003, **29**, 567-597.
13. B. Meredig and C. Wolverton, *Physical Review B*, 2009, **80**, 245119.
14. M. Lundberg, *International Journal of Hydrogen Energy*, 1993, **18**, 369-376.
15. A. Steinfeld, *International Journal of Hydrogen Energy*, 2002, **27**, 611-619.
16. G. Levêque, S. Abanades, J.-C. Jumas and J. Olivier-Fourcade, *Industrial & Engineering Chemistry Research*, 2014, **53**, 5668-5677.
17. M. D. Allendorf, R. B. Diver, N. P. Siegel and J. E. Miller, *Energy & Fuels*, 2008, **22**, 4115-4124.
18. W. C. Chueh, C. Falter, M. Abbott, D. Scipio, P. Furler, S. M. Haile and A. Steinfeld, *Science*, 2010, **330**, 1797-1801.
19. A. H. McDaniel, E. C. Miller, D. Arifin, A. Ambrosini, E. N. Coker, R. O'Hayre, W. C. Chueh and J. H. Tong, *Energy & Environmental Science*, 2013, **6**, 2424-2428.
20. J. R. Scheffe, J. H. Li and A. W. Weimer, *International Journal of Hydrogen Energy*, 2010, **35**, 3333-3340.
21. A. H. McDaniel, A. Ambrosini, E. N. Coker, J. E. Miller, W. C. Chueh, R. O'Hayre and J. Tong, *Energy Procedia*, 2014, **49**, 2009-2018.
22. S. Abanades and G. Flamant, *Solar Energy*, 2006, **80**, 1611-1623.
23. H. Kaneko, T. Miura, H. Ishihara, S. Taku, T. Yokoyama, H. Nakajima and Y. Tamaura, *Energy*, 2007, **32**, 656-663.
24. J. R. Scheffe, D. Weibel and A. Steinfeld, *Energy & Fuels*, 2013, **27**, 4250-4257.
25. A. Demont, S. Abanades and E. Beche, *The Journal of Physical Chemistry C*, 2014, **118**, 12682-12692.
26. C. W. Bale, P. Chartrand, S. A. Degterov, G. Eriksson, K. Hack, R. Ben Mahfoud, J. Melançon, A. D. Pelton and S. Petersen, *Calphad*, 2002, **26**, 189-228.
27. P. Lichty, X. Liang, C. Muhich, B. Evanko, C. Bingham and A. W. Weimer, *International Journal of Hydrogen Energy*, 2012, **37**, 16888-16894.
28. P. G. Loutzenhiser, A. Meier and A. Steinfeld, *Materials*, 2010, **3**, 4922-4938.
29. A. Walsh, S.-H. Wei, Y. Yan, M. Al-Jassim, J. A. Turner, M. Woodhouse and B. Parkinson, *Physical Review B*, 2007, **76**, 165119.
30. J. E. Miller, A. Ambrosini, E. N. Coker, M. D. Allendorf and A. H. McDaniel, *Energy Procedia*, 2014, **49**, 2019-2026.
31. E. J. Palin and R. J. Harrison, *American Mineralogist*, 2007, **92**, 1334-1345.
32. C. Henderson, J. Charnock and D. Plant, *Journal of Physics: Condensed Matter*, 2007, **19**, 076214.
33. A. Navrotsky and O. Kleppa, *Journal of Inorganic and Nuclear Chemistry*, 1967, **29**, 2701-2714.

34. P. J. Linstrom and W. G. Mallard, eds., *NIST Chemistry WebBook, NIST Standard Reference Database Number 69*, National Institute of Standards and Technology, Gaithersburg, MD, 2015.
35. J. Scaranto and H. Idriss, *Topics in Catalysis*, 2014, 1-6.
36. C. L. Muhich, K. C. Weston, D. Arifin, A. H. McDaniel, C. B. Musgrave and A. W. Weimer, *Industrial & Engineering Chemistry Research*, 2014.
37. X. Q. Cao, R. Vassen and D. Stoever, *Journal of the European Ceramic Society*, 2004, **24**, 1-10.
38. R. J. Harrison, S. A. Redfern and H. S. C. O'Neill, *American Mineralogist*, 1998, **83**, 1092-1099.
39. J. R. Scheffe, A. H. McDaniel, M. D. Allendorf and A. W. Weimer, *Energy & Environmental Science*, 2013, **6**, 963-973.
40. G. Kresse and J. Furthmüller, *Physical Review B*, 1996, **54**, 11169.
41. G. Kresse and J. Furthmüller, *Computational Materials Science*, 1996, **6**, 15-50.
42. J. P. Perdew, K. Burke and M. Ernzerhof, *Physical Review Letters*, 1996, **77**, 3865.
43. G. Kresse and D. Joubert, *Physical Review B*, 1999, **59**, 1758-1775.
44. J. Hubbard, *Proceedings of the Royal Society of London Series a-Mathematical and Physical Sciences*, 1963, **276**, 238-+.
45. A. Walsh, S.-H. Wei, Y. Yan, M. M. Al-Jassim, J. A. Turner, M. Woodhouse and B. A. Parkinson, *Physical Review B*, 2007, **76**, 165119.
46. G. Henkelman, A. Arnaldsson and H. Jónsson, *Computational Materials Science*, 2006, **36**, 354-360.
47. E. Sanville, S. D. Kenny, R. Smith and G. Henkelman, *Journal of Computational Chemistry*, 2007, **28**, 899-908.
48. *US Pat.,* US 3330697 A, 1967.
49. D. M. King, J. A. Spencer Ii, X. Liang, L. F. Hakim and A. W. Weimer, *Surface and Coatings Technology*, 2007, **201**, 9163-9171.
50. X. Liang, N.-H. Li and A. W. Weimer, *Microporous and Mesoporous Materials*, 2012, **149**, 106-110.
51. P. Lichty, C. Perkins, B. Woodruff, C. Bingham and A. Weimer, *Journal of Solar Energy Engineering*, 2010, **132**, 011012-011012.

Predicting the Solar Thermochemical Water Splitting Ability and Reaction Mechanism of Metal Oxides: a Case Study of the Hercynite Family of Water Splitting Cycles

Christopher L. Muhich[a†], Brian D. Ehrhart[a], Vanessa A. Witte[a], Samantha L. Miller[a], Eric N. Coker[c], Charles B. Musgrave[a,b*], and Alan W. Weimer[a*]

[a]Department of Chemical and Biological Engineering, University of Colorado, Boulder, Colorado 80309, USA

[b]Department of Chemistry and Biochemistry, University of Colorado, Boulder, Colorado 80309, USA

[c]Sandia National Laboratories, Albuquerque, New Mexico 87123, USA

[*]Corresponding Author: Email addresses: Charles.Musgrave@colorado.edu and Alan.Weimer@colorado.edu

Broader Context

Solar thermal water splitting (STWS) has the potential to efficiently generate renewable hydrogen from water and concentrated sunlight. STWS is typically accomplished using a two-step reduction-oxidation cycle commencing with thermal reduction of a metal oxide to generate O_2 followed by reoxidation of the reduced metal oxide by steam to generate H_2. The thermodynamic and kinetic properties of the metal oxide dictate the viability and efficiency of the STWS process. An optimum metal oxide has not yet been identified, although active searches have been undertaken. Rapid computational assessment of candidate STWS materials has been primarily hindered by the complexity and intensity of calculations necessary for the accurate prediction of the reduction entropies of complex oxides, and oxides that operate via an O-vacancy mechanism, two characteristics of the most promising materials discovered to date. Here, we develop an elegant computational screening method based on O-vacancy formation energies for characterizing the ability of redox materials to split water. We demonstrate this method for rapid screening of novel STWS materials using the hercynite cycle, experimentally confirm its predictions and show that the doped-hercynite cycle is governed by an O-vacancy mechanism. This method could be extended to other redox cycle processes such as chemical looping.